Interior Reflections of a Periodically Forced Equatorial Kelvin Wave[‡]

LEWIS M. ROTHSTEIN, DENNIS W. MOORE[*] AND JULIAN P. MCCREARY[@]

School of Oceanography/J.I.S.A.O., University of Washington, Seattle, WA 98105

(Manuscript received 1 September 1984, in final form 19 February 1985)

ABSTRACT

A fully three-dimensional, wind-forced equatorial model is used to study the effects of the strong near-surface equatorial pycnocline on energy transmission into the deep ocean. The equatorial Kelvin waves forced by a patch of zonal wind oscillating at the annual period are isolated from the complete response, and their energy transmission into the deep ocean is investigated as a function of forcing geometry, pycnocline structure, and the amplitude of deep-ocean mixing. Solutions form well-defined beams of energy that propagate through realistic pycnoclines with surprisingly little reflection. Vertical mixing damps the beams in the direction of their propagation and stretches their longitudinal extent. For sufficiently strong mixing the solutions lose their beamlike character and appear as surface-trapped signals. This result may help to resolve the differences between the solutions found in previous investigations.

1. Introduction

Energetic currents and thermal fluctuations in the deep equatorial oceans have been observed in the Indian Ocean (Luyten and Swallow, 1976; Eriksen, 1980; Luyten, 1982; Luyten and Roemmich, 1982), in the Atlantic Ocean (Weisberg and Horigan, 1981), and in the Pacific Ocean (Eriksen, 1981; Hayes and Milburn, 1980; Hayes, 1981; Leetmaa and Spain, 1981; Lukas and Firing, 1985). The ultimate source of this energy must be the surface wind stress. The direct transmission of wind-forced energy into the deep equatorial ocean will be affected by the presence of the strong equatorial pycnocline. Recently there have been conflicting ideas concerning the amount of energy that is able to penetrate the pycnocline.

Philander (1978) and Philander and Pacanowski (1980) discussed the response of a linear, equatorial ocean model to a forcing that was periodic in both time and longitude, and calculated energy transmission coefficients through a variety of background density structures [see, for example, the discussion of Eq. (16)]. They found that, for a realistic choice of density structure, there was considerable reflection of energy from the pycnocline at all wavelengths. Philander and Pacanowski (1981) studied the response of an oceanic general circulation model to zonal

winds periodic in time. The surface currents were much larger than the deep currents, and the authors concluded that most of the energy generated by the wind was trapped near the surface by reflections from the pycnocline, as suggested by their earlier work.

McCreary (1984) forced a linear, continuously stratified ocean model with a zonal wind patch oscillating at the annual period. One of the solutions was for a background density stratification with a sharp, near-surface pycnocline. A dominant feature of this solution (and others) was the excitation of Kelvin waves by the wind; these waves superposed to form a well-defined beam of energy that propagated both eastward and downward into the deep ocean. In apparent contradiction to the studies mentioned in the previous paragraph, the beam appeared to pass through the model pycnocline very efficiently with only weak internal reflections. The solution was complicated by the reflection of Rossby waves from the eastern boundary. These waves also superposed to generate beams, thereby forming the indirect route that was the ultimate source of deep energy in the model. McCreary compared his solutions to those of Philander and Pacanowski (1981), and noted that aspects of the deep response of both models were similar; in particular, he suggested that there was a Kelvin beam and a reflected Rossby beam in their deep solutions.

The purpose of this paper is to examine in detail how the equatorial pycnocline affects the propagation of energy into the deep ocean. The paper focuses on the radiation of Kelvin waves from a wind patch oscillating at a period of one year, but our results are also applicable to other periods and to the radiation

* Permanent affiliation: Joint Institute for Marine and Atmospheric Research, University of Hawaii, Honolulu, HI 96822.

@ Permanent affiliation: Nova University Oceanographic Center, Dania, FL 33004.

‡ Contribution Number 21 of the Joint Institute for the Study of the Atmosphere and Ocean, University of Washington.

of nondispersive Rossby waves (see the remarks at the end of Section 2b). The eastern ocean boundary is neglected in order to avoid complications that are caused by reflected Rossby waves. The ocean model is linearized about a background density field and includes vertical mixing of both momentum and heat. A variety of background density fields are adopted with pycnoclines that range in complexity from very simple analytical forms to an observed structure. In addition, forcing geometry and the strength of mixing are varied.

Important results are the following. For realistic choices of pycnocline structures most of the wind-forced energy propagates directly through the pycnocline and enters the deep ocean. Sufficiently strong mixing, however, destroys the beamlike character of the solution, and creates the appearance of surface trapping. Thus, vertical mixing may be the reason for the apparent surface trapping in the Philander and Pacanowski (1981) model, not internal reflections from the pycnocline as they suggest.

2. The model

a. Equations and boundary conditions

The model equations are the linear set

$$u_t - \beta y v + p_x/\rho_0 = F(x, y, z, t) + (\nu u_z)_z,$$

$$v_t + \beta y u + p_y/\rho_0 = G(x, y, z, t) + (\nu v_z)_z,$$

$$u_x + v_y + w_z = 0,$$

$$p_z = -\rho g,$$

$$\rho_t - \frac{\rho_0}{g} w N_b^2 = (K\rho)_{zz}, \tag{1}$$

where all variables have their usual definitions. The equations are linearized about a background density state $\rho_b(z)$ with an associated Väisälä frequency N_b, and ρ_0 is the average value of $\rho_b(z)$ over the water column. Choosing the Coriolis parameter to be βy is the equatorial beta-plane approximation. There is no lateral diffusion; however Section 3a has a brief qualitative discussion of how we expect lateral diffusion to affect the solutions.

The mixing of heat and momentum have unconventional forms. The mixing of heat is $(K\rho)_{zz}$, rather than $(K\rho_z)_z$, and the mixing coefficients are

$$\nu(z) = K(z) = A/N_b^2(z) \tag{2}$$

where A is a constant. These forms are chosen so that analytical solutions can be represented as expansions of vertical modes. Solutions from other models using this particular form for vertical mixing give quite realistic flow fields (McCreary, 1981) and SST fields (Rothstein, 1984), and suggest that results are not very sensitive to this particular form of vertical mixing. McPhaden (1981) discusses implications of

various forms of vertical diffusion on equatorial dynamics.

Surface and bottom boundary conditions are

$$\nu u_z = \nu v_z = w = K\rho = 0 \quad \text{at} \quad z = 0, -D. \tag{3}$$

There is a no-stress condition at the ocean surface, because we assume that all the stress introduced by the wind is taken up in the terms F and G.

The model is forced by a body force with the separable form

$$F = \tau_0 X(x) Y(y) Z(z) e^{-i\sigma t}, \quad G = 0 \tag{4}$$

where $\sigma = 2\pi$ year^{-1} and $\tau_0 = 0.5$ dyn cm^{-2}. Meridional wind stress is neglected, since that component does not generate Kelvin waves. The zonal structure of the forcing is

$$X(x) = \begin{cases} \sin \dfrac{\pi(x - x_w)}{\Delta x}, & x_w \leqslant x \leqslant x_e \\ 0, & x \text{ elsewhere,} \end{cases} \tag{5}$$

where $x_e = x_w + \Delta x$, $x_w = -47\,500$ km and $\Delta x = 5000$ km. (The choice of these basin parameters will be discussed shortly.) The meridional structure is

$$Y(y) = \left[1 + \left(\frac{y}{\Delta y}\right)^2\right] \exp\left[-\left(\frac{y}{\Delta y}\right)^2\right], \tag{6}$$

and $\Delta y = 1000$ km. With this choice of $Y(y)$, the wind field is symmetrical about the equator, is essentially y-independent near the equator, and decreases markedly for $y \geqslant \Delta y$. Thus, the ocean is forced by a patch of zonal wind with a zonal and meridional extent of Δx and Δy, respectively. The vertical structure is

$$Z(z) = \theta(z + H)/H, \tag{7}$$

where $\theta(z + H)$ is a step function, so that the wind stress is distributed uniformly throughout a surface mixed layer of thickness H. For most solutions, $H = 50$ m; the sole exception is for the solutions discussed in Section 3c where $H = 30$ m.

b. The solution

With the above choice for F, the system is separable in both the y and z coordinates, and the resulting differential equation in x alone can be solved easily by Fourier-transform techniques (McCreary, 1981; Rothstein, 1984). The solution is expressed as a sum of all possible waves that can be generated by the wind patch. The pressure and zonal velocity fields due to Kelvin waves alone are

$$p = \sum_{n=1}^{N} \left\{ \frac{\tau_{0n}}{2} [Y]_{0n} \int_{-\infty}^{x} e^{-i(\omega_n/c_n)x'} X(x') dx' \right\}$$
$$\times \phi_0(\eta_n) \psi_n(z) e^{i\omega_n(x/c_n - t)}$$
$$\equiv \sum_{n=1}^{N} p_n(x) \phi_0(\eta_n) \psi_n(z) e^{i\omega_n(x/c_n - t)},$$

$$u = \sum_{n=1}^{N} \frac{p_n(x)}{c_n} \phi_0(\eta_n) \psi_n(z) e^{i\omega_n(x/c_n - t)}, \tag{8}$$

where $\omega_n = \sigma + iA/c_n^2$. The ψ_n's are the eigenfunctions that satisfy

$$\frac{d}{dz}\left\{\frac{1}{N_b^2}\frac{d}{dz}\right\}\psi_n + \frac{\psi_n}{c_n^2} = 0,$$ (9a)

subject to the boundary conditions

$$\frac{1}{N_b^2}\frac{d\psi_n}{dz} = 0 \quad \text{at} \quad z = 0, -D,$$ (9b)

and they are normalized so that $\psi_n(0) = 1$. The function, $\phi_0(\eta_n)$, is the gravest Hermite function given by

$$\phi_0(\eta_n) = \pi^{-1/4}e^{-\eta n^2/2}$$ (10)

where $\eta_n = (\beta/c_n)^{1/2}y$, the Hermite expansion coefficient of Y is

$$[Y]_{0n} = \int_{-\infty}^{\infty} Y\phi_0(\eta_n)d\eta_n,$$ (11)

and the coupling of each mode to the wind is

$$\tau_{0n} = \frac{\tau_0}{H}\frac{\int_{-H}^{0}\psi_n dz}{\int_{-D}^{0}\psi_n^2 dz}.$$ (12)

Finally, $N = 50$ for all cases, a number sufficiently large for solutions to be well converged.

Long-wavelength Rossby waves, that approximately satisfy the dispersion relation

$$k_{ln} = -\left(\frac{\omega_n}{c_n}\right)(2l + 1)$$

where l is a positive integer, are also generated by the wind patch. The expressions for the flow field due to these waves are similar in form to (8), the essential difference being that ω_n/c_n is replaced by k_{ln} in the exponentials and the lower limit of integration is $+\infty$. Thus, the structure of the Rossby wave contribution is identical to that of the solutions found here with the replacements $\omega_n \rightarrow \omega_n/(2l + 1)$ and $x \rightarrow -x$.

c. Kelvin beams

According to WKB theory, approximate solutions to (9) are $\psi_n(z) = N_b^{1/2}\cos(\int^z m dz)$ where $m = N_b/c_n$ is a local vertical wavenumber. Let $b = N_b/N_{bz}$ measure the vertical scale of $N_b(z)$. Then the WKB solution is valid to order $(mb)^{-2}$. Since the cosine above can be written as the sum of two complex exponentials, it is apparent that each vertical mode consists of a wave with phase propagating upward and one with phase propagating downward.

Energy associated with packets of these waves travels along ray paths. The dispersion relation for Kelvin waves is $\sigma = kc_n = k(N_b/m)$. The slope of ray paths is therefore

$$\tan\theta_e = \frac{\partial\sigma/\partial m}{\partial\sigma/2k} = \mp\frac{\sigma}{N_b},$$

where the upper (lower) sign holds for waves with upward (downward) phase propagation. Thus, when phase propagates upward, energy propagates downward and to the east for Kelvin waves. The slopes are typically quite small; for example, with a typical value of $N_b = 0.005$ s^{-1}, $\sigma/N_b = 400$ m/10 000 km. When the forcing has a simple structure, like it does here, the radiation field forms well-defined beams that carry energy into the deep ocean (McCreary, 1984).

When there is a sharp pycnocline, so that b is a small number at some level in the water column, the WKB approximation is not valid for low-order vertical modes. The effect is that energy can reflect from the pycnocline (Philander, 1978), rather than follow ray paths through it. The purpose of this study is to examine this reflection process in detail.

3. Results

This section shows solutions for various choices of background stratification, forcing geometry and mixing strength. As we shall see, solutions vary considerably with the choice of the model parameters. For all solutions, we plot contours of the zonal energy-flux density, $\lambda(x, z) = \text{Re}(up^*)$, in the equatorial plane. (In this expression p^* is the complex conjugate of p and $\text{Re}(up^*)$ is the real part of up^*). This quantity shows clearly the location of the Kelvin beams and, as discussed next, also provides a measure of the amount of energy that is transmitted both zonally and vertically along the equator.

It is useful to define a measure of the contributions of individual modes to the solutions. The total zonal energy flux on the equator is

$$\Lambda(x) = \int_{-D}^{0}\lambda dz = \sum_{n=1}^{N}\Lambda_n(x),$$

where according to (8),

$$\Lambda_n(x) = (|p_n(x)|^2/c_n\pi^{1/2})\int_{-D}^{0}\psi_n^2 dz.$$ (13)

The quantity $\Lambda_n(x)$ measures which vertical modes contribute to the solution. Note that for inviscid solutions $\Lambda_n(x)$ is constant east of the wind patch. In all cases, plots of $\Lambda_n(x)$ are evaluated at $x = -37\,500$ km., far to the east of the directly forced region.

For inviscid solutions, λ is also a measure of the vertical energy flux associated with a beam. The inviscid and time-independent energy equation implies that $\oint_c d\text{l}\cdot\text{Re}(\bar{u}p^*) = 0$, where n is a unit vector normal to the path of integration c. It follows that $\int_{l_1}\lambda dz = -\int_{l_2}\text{Re}(wp^*)dx$, where l_1 and l_2 are vertical and horizontal contour lines that extend across the beam. Thus the total downward energy flux of the beam is equal to it's total eastward energy flux.

For inviscid solutions and when N_b is constant, the structure of a beam does not vary (as in Fig. 1). In that case, the maximum value of λ in the beam is
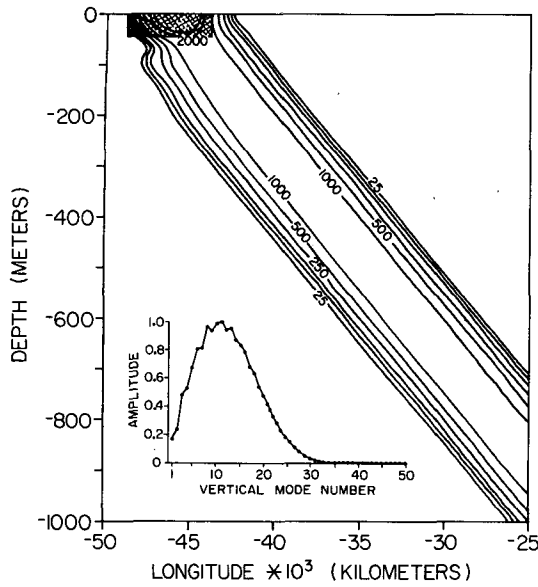
FIG. 1. Contours of λ for an inviscid ocean with a constant Väisälä frequency, N_b = 0.005 s^{-1}. The shaded area indicates the region of forcing by the wind. Kelvin waves superpose to form a well-defined beam that descends into the ocean at the angle θ_e = tan$^{-1}(\sigma/N_b)$. The maximum value of λ is 1650 cm^3 s^{-3}. (Inset: Spectral representation of the solution normalized by the maximum value of $\Lambda_n(x)$. $\Lambda_n(x)$ is evaluated at x = −37 500 km. The most strongly excited Kelvin waves correspond to the n = 11 mode).

directly proportional to $\int_h \lambda dz$. The Väisälä frequency has the same constant value above and below the pycnocline for most of the inviscid solutions found here, the sole exception being the solution in Fig. 11. For these solutions, let λ_a and λ_b be the maximum values of λ above (but away from the directly forced region) and below the pycnocline, respectively; then the ratio λ_b/λ_a is the transmission coefficient of energy through the pycnocline.

a. Solutions for constant $N_b(z)$

This subsection considers the propagation of Kelvin beams through a linearly stratified ocean. Since these cases lack a pycnocline, the WKB approximation is exact, and there are no interior reflections of the beam. Nevertheless, these solutions are useful for illustrating other basic properties of the Kelvin beams. In particular, the effects of forcing geometry and the strength of mixing on Kelvin beams are discussed.

Figure 1 shows λ along the equator and Λ_n when the ocean is inviscid and N_b has a constant value of 0.005 s^{-1}. The shaded region represents the region of wind forcing. Because the beam slope θ_e is small, the zonal extent of the plot in Fig. 1 is 25 000 km so that we might track the beam into the deep ocean. (To obtain the beam penetration depth in realistic basins, all one needs to do is read the depth in Fig. 1 corresponding to the desired zonal extent of the

basin.) Because there is no mixing, the beam radiates into the deep ocean with no loss of energy. A considerable number of modes contribute to the solution; Λ_n reaches a peak for n = 11, and is effectively zero only for $n \gtrsim 35$.

It is visually apparent that the zonal extent of the beam L is larger than the length of the forcing region Δx. Figure 2 illustrates schematically why this property must be so. The hatched area indicates the region of forcing by the wind. Both upward- and downward-sloping rays are generated at every point in the region. Downward-sloping rays are shown from each corner of the region. An upward-sloping ray is shown leaving the lower east corner of the region; it reflects from the ocean surface as another downward-propagating ray. It is evident in Fig. 2 that the zonal extent of the beam is

$$L = \Delta x + 2H \tan^{-1}\theta_e \approx \Delta x + 2H \frac{N_b}{\sigma}. \quad (14)$$

Thus, beam length depends on the forcing geometry. Note that when θ_e is a small angle, as it is for all the solutions found here, L is affected by H as well as Δx. The vertical extent of the beam is

$$T = L \tan\theta_e \approx \Delta x \frac{\sigma}{N_b} + 2H, \quad (15)$$

and so is also sensitive to forcing geometry. (In fact, the beam in Fig. 1 is really somewhat wider and thicker even than these estimates. This broadening occurs because the radiation problem is fully three dimensional, involving y as well as x and z.)

Figure 3 shows Λ_n for two other inviscid solutions with H = 25 meters and 100 meters. As H increases, Λ_n peaks at ever smaller values of n. This dependence on H makes sense, since as H increases the beam becomes thicker and so fewer vertical modes are needed to resolve it. There is a similar dependence of Λ_n on Δx.
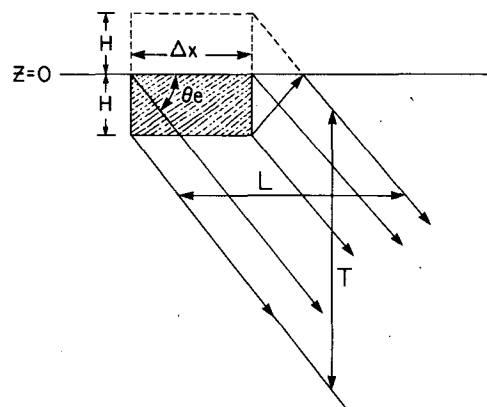

FIG. 2. Schematic diagram showing several ray paths leaving the forcing region (shaded area). The zonal extent and thickness of the beam are related to θ_e and H according to (14) and (15).
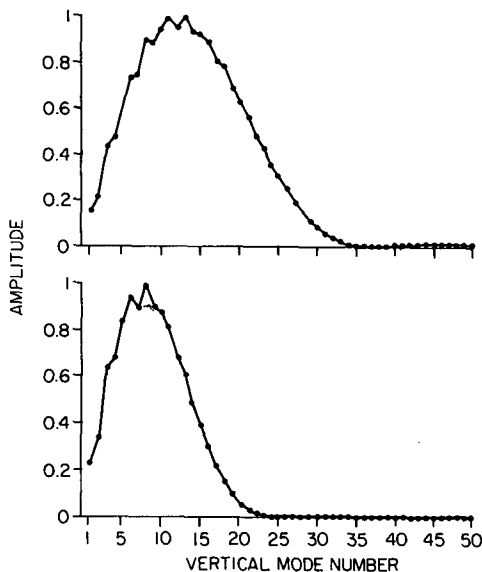
FIG. 3. Spectral representations of solutions for $H = 25$ meters (upper panel) and for $H = 100$ meters (lower panel). As H increases Λ_n peaks at increasingly lower wavenumbers.

Figure 4 shows how vertical mixing affects the Kelvin beam. Both solutions are comparable to the one in Fig. 1, except that $\nu = K = 1$ cm^2 s^{-1} and 10 cm^2 s^{-1} in the upper and lower panels, respectively. Two important modifications of the inviscid solutions are evident. As expected, the beam decays as it propagates into the deep ocean. In addition, the longitudinal extent of the beam increases with increasing friction, that is, the signal can be found further downstream in the upper layers for larger mixing amplitudes.

The solution with large mixing is strongly surface trapped. If the background stratification had a near-surface pycnocline, it would have been easy to mis-interpret the surface-trapping as being due to an interior reflection of the beam. Values of vertical mixing coefficients in the Philander and Pacanowski (1981) study were $\nu = 10$ cm^2 s^{-1} and $K = 1$ cm^2 s^{-1}. Thus, the surface trapping in their solution may have been due to the presence of vertical mixing rather than to pycnocline reflections (also see the discussion of Figs. 11–14 in Section 3c).

To understand why the longitudinal extent of the signal increases with stronger vertical mixing, we turn to the spectral plots for the two cases of Fig. 4, shown in the inset of Fig. 4. As mixing increases, the higher-order modes are increasingly damped out of the solution, thereby shifting the spectrum toward the lower vertical modes. Since these modes radiate away from the forcing region with wavelengths that are longer than (14), the beam spreads zonally.

Although horizontal mixing is not included in this model, its effects on the solution must be quite similar to the effects of vertical mixing. According to (10),

the meridional scale of a particular Kelvin wave decreases with increasing mode number. Thus, horizontal mixing will preferentially damp higher-order vertical modes, just as vertical mixing does. It follows that the inclusion of horizontal mixing will act to broaden both the vertical and zonal extent of the beam as it propagates into the deep ocean.

b. Solutions for idealized $N_b(z)$

We now consider the propagation of Kelvin beams through oceans in which N_b varies. The important effect is that beams are partially reflected by pycno-clines. To examine the reflection process in detail, a series of pycnocline structures are selected that increase in complexity from simple jumps in N_b to more realistic shapes. In order to isolate the surface trapping that is due to pycnocline reflections alone, there is no diffusion for any of the solutions in this subsection.

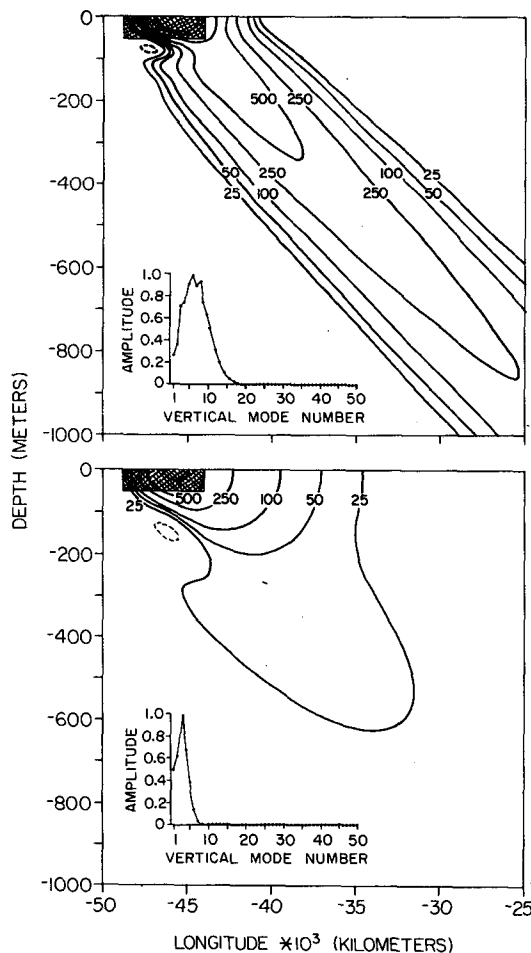Figure 5 shows the five profiles of N_b discussed

FIG. 4. As in Fig. 1, except with $\nu = 1$ cm^2 s^{-1} (upper panel) and $\nu = 10$ cm^2 s^{-1} (lower panel). As ν increases energy is increasingly confined near the ocean surface and Λ_n peaks at increasingly lower wavenumbers.
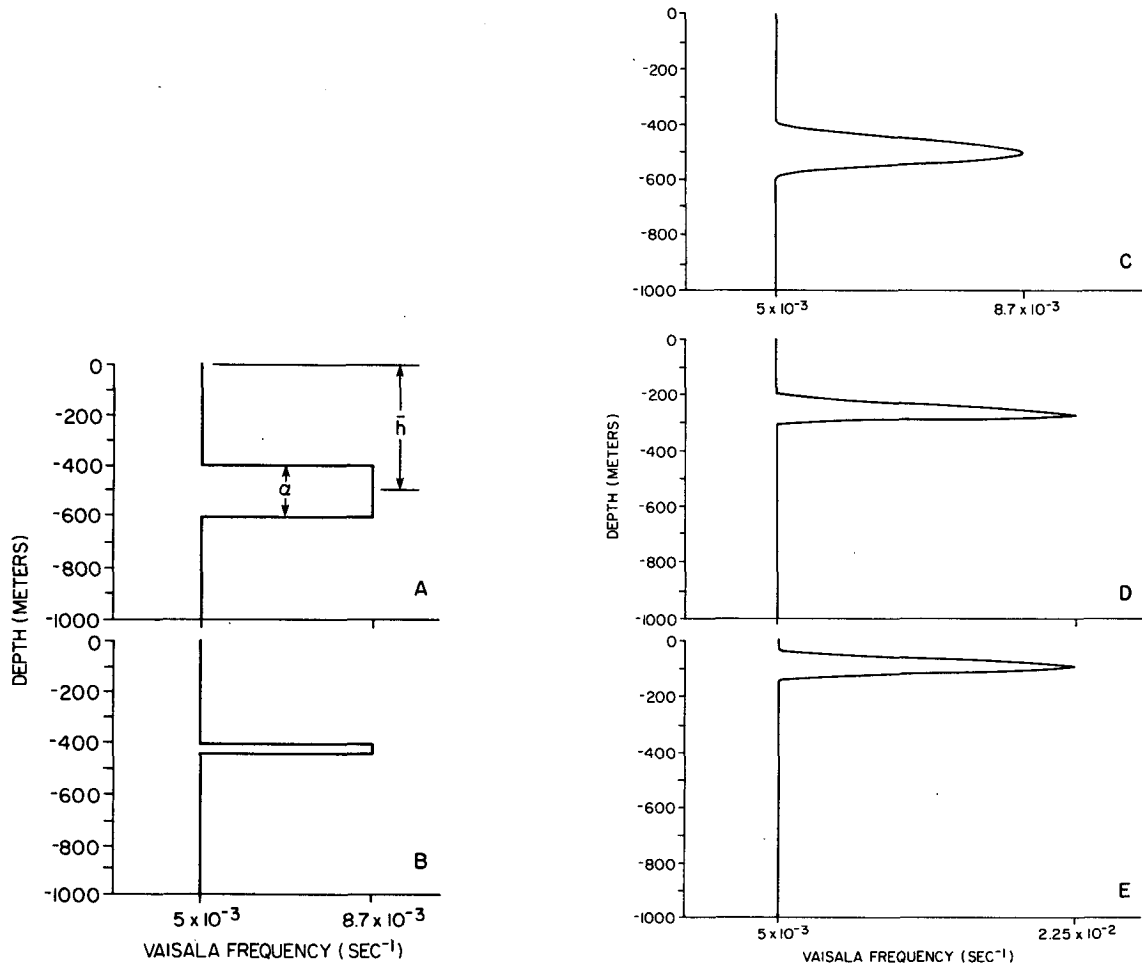
FIG. 5. Profiles of $N_b(z)$ for cases 1–5 in panels (A)–(E), respectively.
See Section 3b for precise definitions of these profiles.

here. The first two cases are simple jumps in N_b of the form

$$N_b = \begin{cases} N_2, & |z + \bar{h}| < \alpha/2 \\ N_1, & |z + \bar{h}| \geq \alpha/2, \end{cases}$$

where $N_1{}^2 = 2.5 \times 10^{-5}$ s^{-2}, $N_2{}^2 = 7.5 \times 10^{-5}$ s^{-2}, $\bar{h}$ = 500 m. and α = 200 m. for case 1, whereas $\bar{h}$ = 410 m. and α = 20 m. for case 2. The last three cases are pycnoclines with smooth edges described by

$$N_b = \begin{cases} N_1 + \dfrac{(N_2 - N_1)}{2}\left[1 - \cos\dfrac{2\pi(z + \bar{h})}{\alpha}\right], \\ \hspace{3cm} |z + \bar{h}| < \alpha/2 \\ N_1, \quad |z + \bar{h}| \geq \alpha/2. \end{cases}$$

For case 3 the parameter values are the same as case 1. For case 4, they are $N_1{}^2 = 2.5 \times 10^{-5}$ s^{-2}, $N_2{}^2$ = 5×10^{-4} s^{-2}, $\bar{h}$ = 250 m and α = 100 m. Case 5 has the same values as case 4, except that $\bar{h}$ = 90 m.

1) SOLUTIONS FOR JUMPS IN N_b

Plots of λ for the Kelvin beams corresponding to cases 1 and 2 are shown in the upper and lower panels of Fig. 6, respectively. (Note in this figure, and all subsequent similar figures, that the zonal extent of the plot is twice that of Fig. 1.) Part of the original beam (the primary beam) is reflected as it encounters the first N_b discontinuity at $z = -400$ m, and another part is reflected at the second discontinuity at $z = -600$ m. In case 2 the jumps in N_b are sufficiently close that both reflected beams overlap. Reflected beams (secondary beams) go through additional reflections further eastward, with a continuing loss of amplitude as parts of them are reflected into other secondary beams.

When N_b has a jump from N_1 to N_2, the energy-transmission ratio across the interface can be calculated analytically, and is given by

$$4N_1N_2/(N_1 + N_2)^2 \tag{16}$$

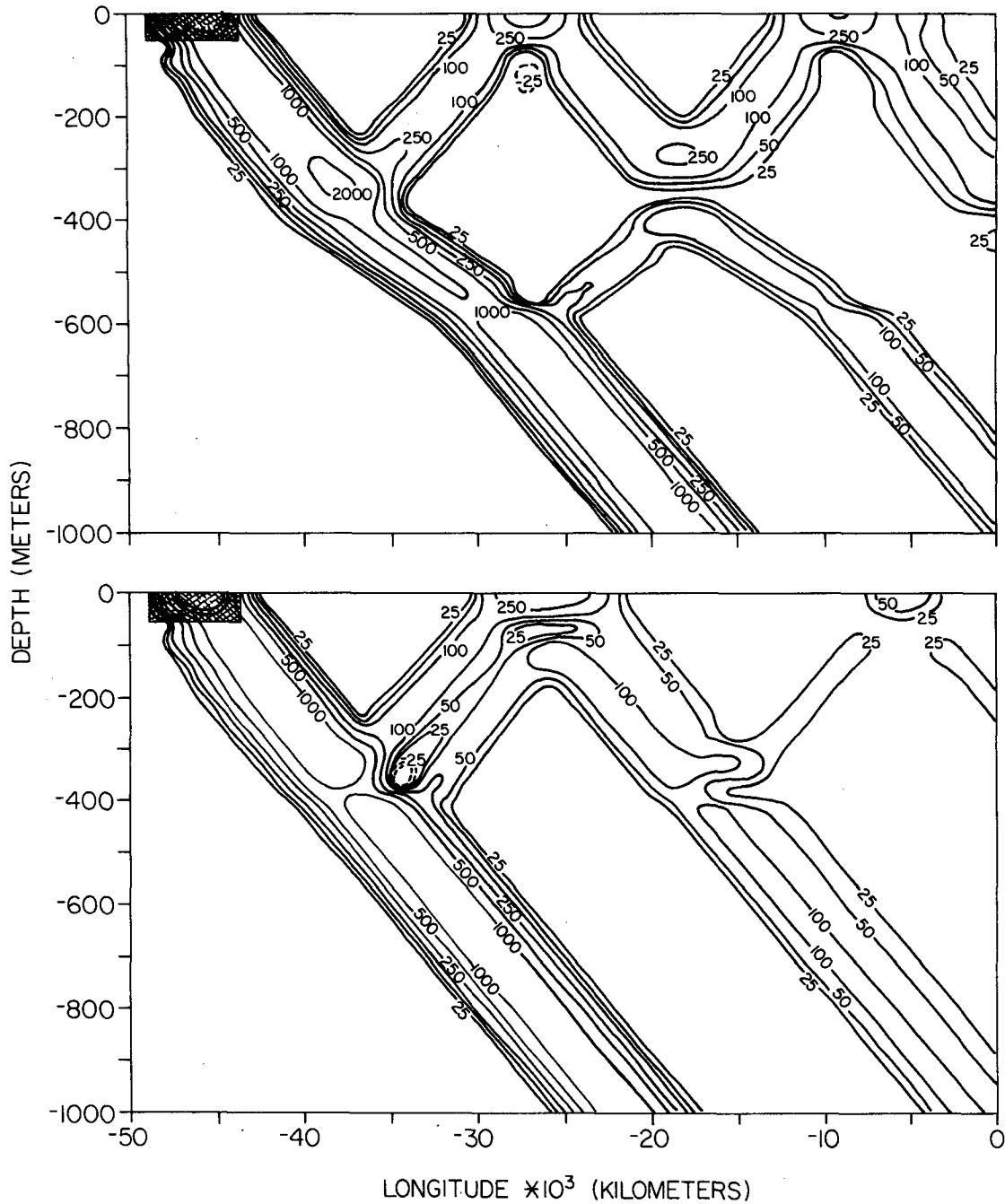(Philander, 1978). The choice of N_b in cases 1 and 2

FIG. 6. Contours of λ for the profile of $N_b(z)$ of case 1 (upper panel) and of case 2 (lower panel). A primary beam propagates directly into the deep ocean. A number of secondary beams are generated by reflections at levels where N_b changes. In case 1, values of λ_a and λ_b are 1975 cm³ s⁻³ and 1700 cm³ s⁻³ and in case 2 they are 1700 cm³ s⁻³ and 1525 cm³ s⁻³ giving transmission coefficients of 86 and 89%, respectively. These coefficients are in agreement with the predictions of Eq. (16).

consists of two jumps, and the direct transmission past this pycnocline can be found by applying (16) twice, once at each interface. For the values of N_1 and N_2 used in cases 1 and 2, (16) implies that 86.5% of the energy of the primary beam will be transmitted directly to the deep ocean. The solutions in Fig. 6 are consistent with this result; $\lambda_a = 1975$ cm³ s⁻² and $\lambda_b = 1700$ cm³ s⁻³ giving an 86% transmission coefficient for case 1 and $\lambda_a = 1700$ cm³ s⁻³ and $\lambda_b = 1525$ cm³ s⁻³ resulting in an 89% transmission coefficient for case 2. (In fact, the transmission coefficient in case 2 is slightly greater than expected. The

reason for this increase is that the N_b jumps are so close together. As a result, one secondary beam, one that reflects first from the lower interface and then from the upper interface, overlaps the primary beam in the deep ocean. There is also destructive interference above the first N_b jump.)

It is evident, however, that secondary beams also carry energy into the deep ocean. Eventually, these secondary beams ensure that all the energy generated by the wind is carried into the deep ocean. No energy ever remains trapped in the upper ocean. This conclusion is a general one, holding for all subsequent solutions as well.

2) SOLUTIONS FOR CONTINUOUSLY VARYING N_b

The structure of N_b in case 3 is essentially that of case 1 except that N_b is smoothly varying. Figure 7 shows the profiles of λ for case 3. A comparison with the solution of case 1 (upper panel of Fig. 6) indicates that when N_b is smoothly varying there is a continuous reflection of energy throughout the region of the pycnocline. The amplitude of the primary beam in the deep ocean, however, is comparable to that of case 1, indicating that the smoothly varying profile does not reflect significantly less energy. ($\lambda_a = 1625$ cm^3 s^{-3} and $\lambda_b = 1535$ cm^3 s^{-3} giving a 94% transmission coefficient in this case).

Cases 4 and 5, shown in Figs. 8 and 9 respectively, investigate how an increase in strength of the pycnocline and a change in it's depth affect the response. The structure of the pycnocline in case 4 is fairly

realistic, except that it is located at a depth of 250 meters, far from the directly forced surface layer. Due to the increase in the amplitude of N_b, considerably less primary-beam energy propagates through the idealized pycnocline than in Fig. 7; $\lambda_a = 1400$ cm^3 s^{-3} and $\lambda_b = 887$ cm^3 s^{-3} so that the transmission coefficient decreases to 63%. The stronger reflected beams form a complex interference pattern above the pycnocline; for example, there are regions where beams interfere to generate negative values of λ. The pycnocline in case 5 is like that in case 4 except that it is located near the surface. Primary-beam energy is only slightly affected in the deep ocean; as for the solution in Fig. 8, $\lambda_b = 855$ cm^3 s^{-3} and $\lambda_b/\lambda_a = 61\%$. The structure of the solution above the pycnocline, however, differs considerably between Figs. 8 and 9.

The shallow pycnocline case is the most realistic of our idealized cases, and the solution in Fig. 9 is quite similar to the solution for the observed density profile discussed in the next subsection. We conclude from these last two cases that the model is capable of reflecting large amounts of energy from a realistic pycnocline, but that even for very sharp pycnoclines considerable energy still propagates directly through into the deep ocean.

c. Realistic stratification

For all the solutions in this subsection, the background density profile is taken from the Hawaii-to-Tahiti Shuttle Experiment (Wyrtki, et al., 1981; Lukas and Firing, 1985). This profile is based upon all CTD
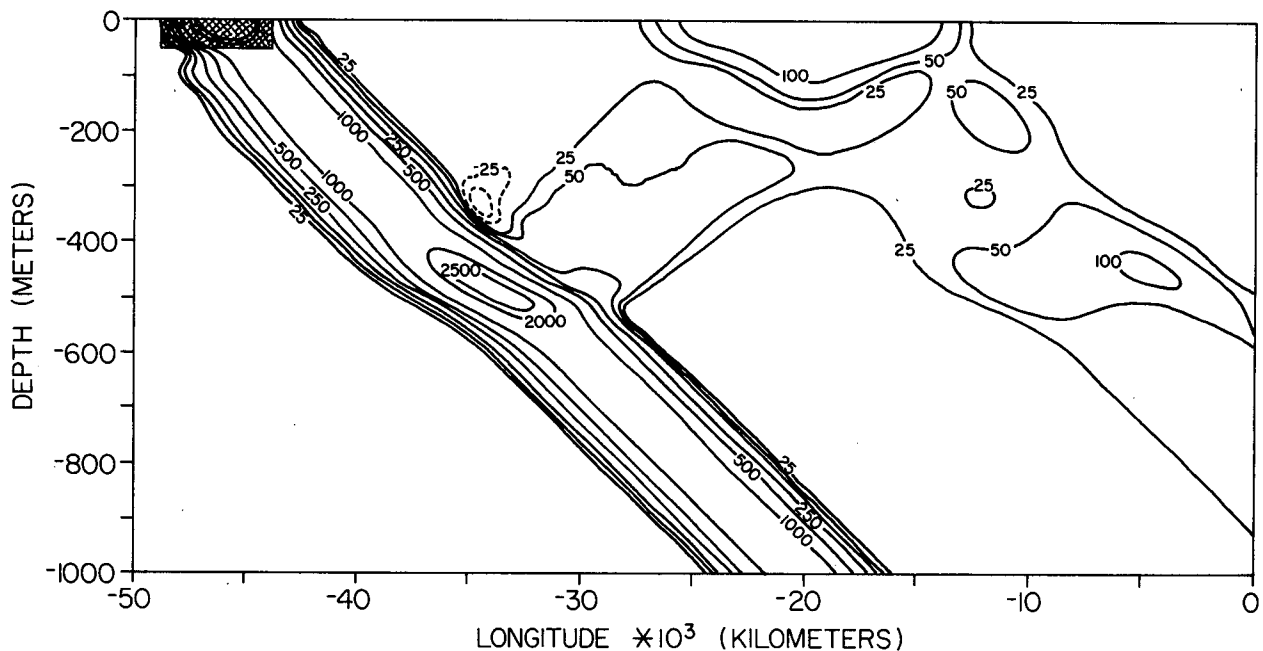

FIG. 7. As in Fig. 6 except for the stratification of case 3. Values of λ_a and λ_b are 1625 cm^3 s^{-3} and 1535 cm^3 s^{-3}, respectively, so that the transmission coefficient of the primary beam is 94%.
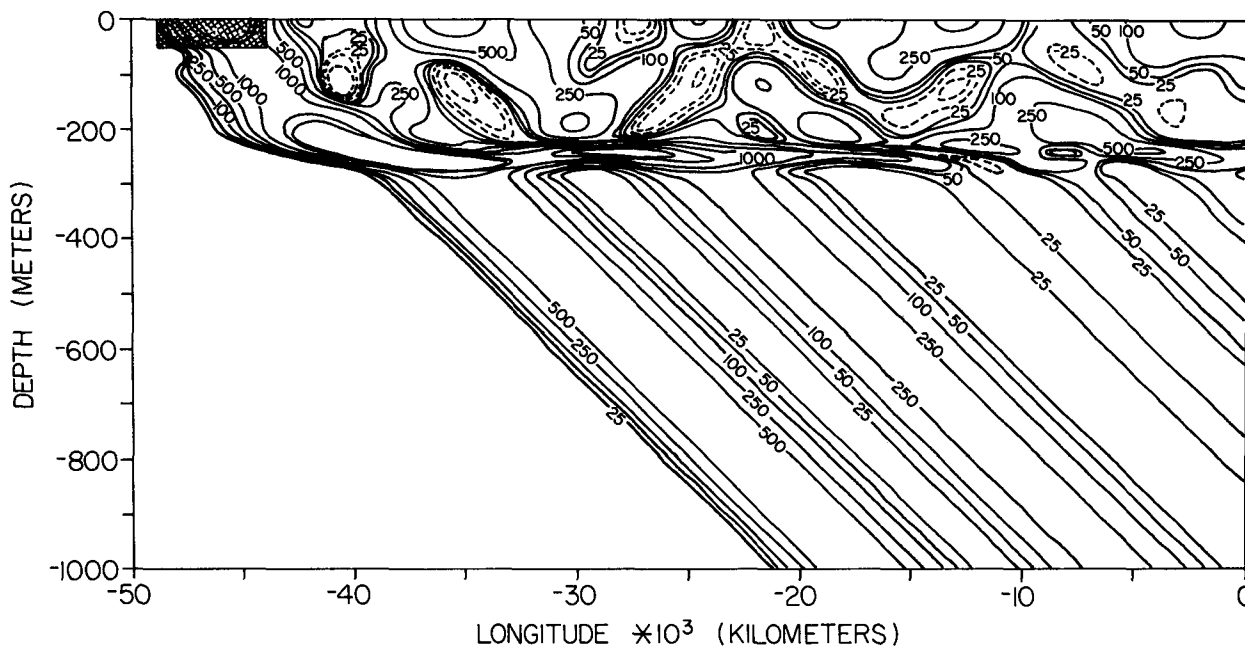
FIG. 8. As in Fig. 6 except for the stratification of case 4. Values of λ_a and λ_b are 1400 cm^3 s^{-3} and 887 cm^3 s^{-3}, respectively, so that the transmission coefficient of the primary beam is 63%.

stations between 5°S–5°N, at 150°W and 158°W. The depth of the ocean in the Shuttle profile region is 4400 meters. The Väisälä frequency in the upper 700 meters is shown in Fig. 10.

The inviscid Kelvin beam is pictured in Fig. 11. The primary result here is that WKB theory works surprisingly well, with the beam of energy following it's ray path through the region where N_b varies rapidly. (The WKB ray path is the heavy dashed line in Fig. 11). Most of the primary beam just refracts through the changing background state and penetrates into the deep ocean. As expected, reflection does take place in the region of the pycnocline. The response spectrum for this case (inset of Fig. 11) shows that,
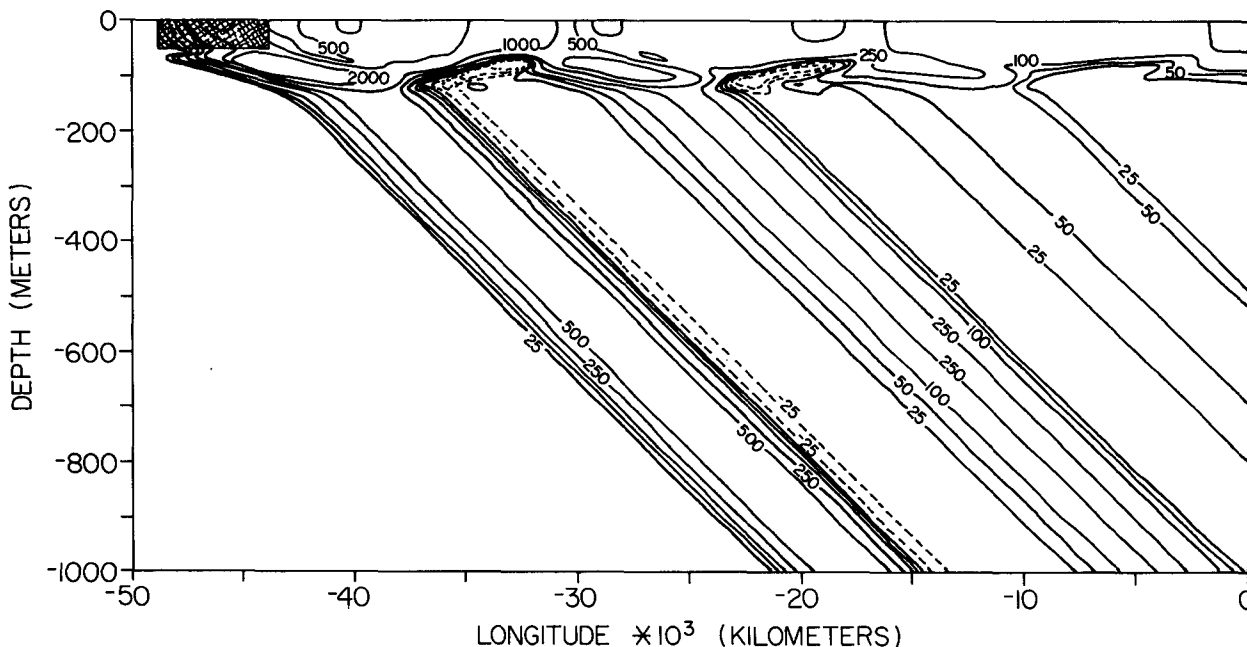
FIG. 9. As in Fig. 6 except for the stratification of case 5. Values of λ_a and λ_b are 1400 cm^3 s^{-3} and 855 cm^3 s^{-3}, respectively, so that the transmission coefficient of the primary beam is 61%.
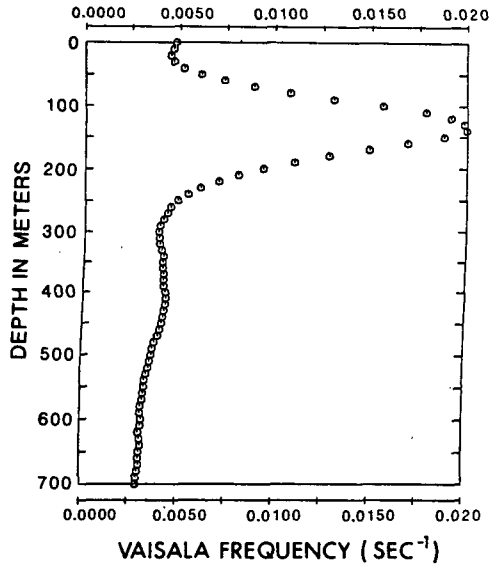
FIG. 10. Brunt–Väisälä frequency distribution for all Hawaii-to-Tahiti Shuttle CTD stations between 5°S and 5°N, 150 and 158°W.

although the lowest mode is dominant, there are significant contributions from the higher modes.

Note, in Fig. 11, that λ decreases markedly with depth, giving the appearance that the transmission coefficient drops in the deep ocean. However, λ is no

longer directly proportional to downward energy flux because N_b is not constant in the deep ocean, thereby broadening the beam vertically. In fact, the downward energy flux in Fig. 11 is constant in the deep ocean.

How is this solution affected by the inclusion of depth-dependent vertical mixing of the form (2)? Figure 12 shows how ν (and K) varies with depth when A is set such that the deep-ocean mixing is of order 10 cm^2 s^{-1}. This large value was chosen to demonstrate clearly the effects of friction on the Kelvin beam. Figure 13 shows the solution for this choice of ν. The primary beam no longer penetrates very far into the deep ocean, but is rapidly damped by the large values of the deep eddy viscosity. The response spectrum is now dominated by contributions from the low order modes. The solution gives the impression that energy is trapped above the pycnocline by interior reflections, but that is not the case, as is evident in Fig. 11. As mentioned before, damping is also a likely reason that so much energy appears to remain trapped above the pycnocline in the model of Philander and Pacanowski (1981).

Figure 14 shows the solution when A is decreased by an order of magnitude so that in the deep ocean ν has the value of 1 cm^2 s^{-1}, a typical estimated value / that is commonly used to model deep ocean diffusion. The Kelvin beam is much more apparent in the deep ocean, although it is somewhat weaker than the inviscid case. We therefore conclude that for typical
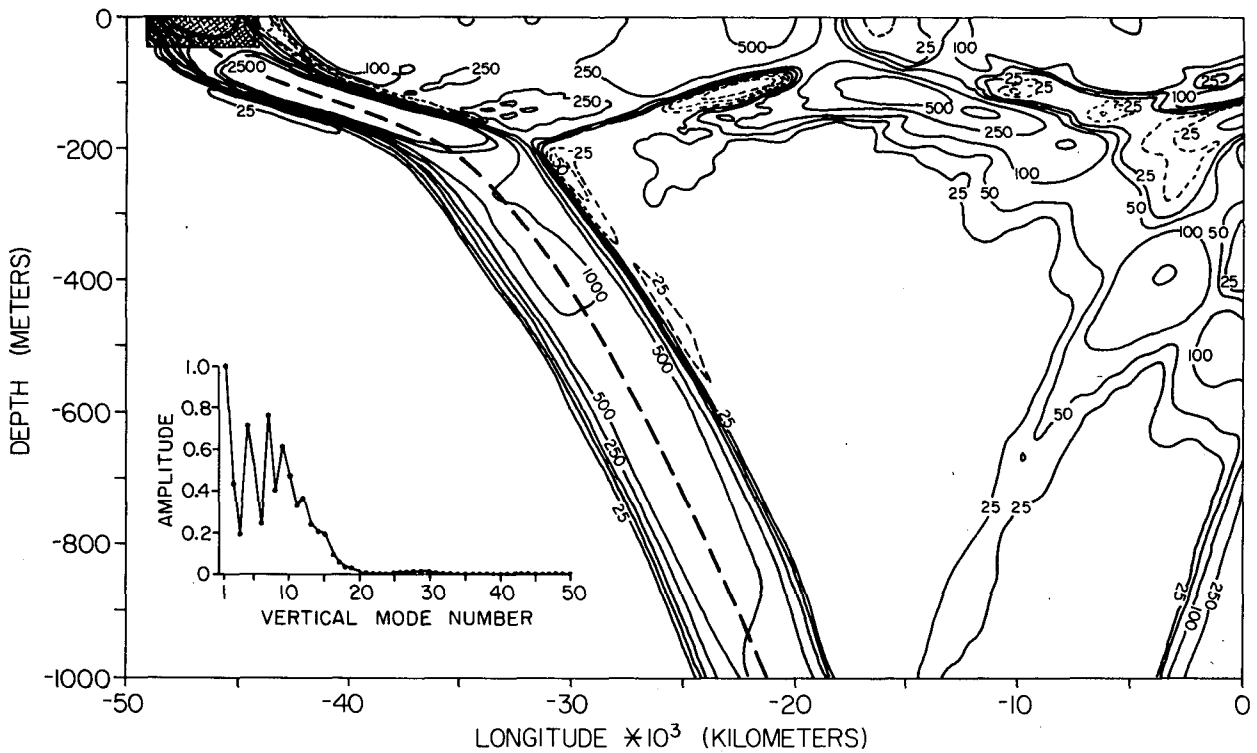

FIG. 11. As in Fig. 1, except for the Hawaii-to-Tahiti Shuttle background stratification. Because N_b decreases in the deep ocean, the maximum value of λ is no longer a measure of downward energy flux. Even though λ decreases with depth, the downward energy flux is constant below the pycnocline in this inviscid solution. (The heavy dashed line is the WKB ray path).
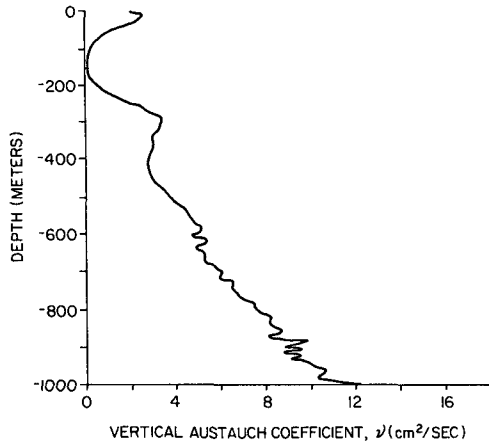
FIG. 12. Variation of ν and K with depth for the large-friction case.

values of vertical mixing the integrity of the Kelvin beam in the deep ocean is not destroyed, and that most of the forced signal will penetrate the pycnocline.

4. Summary and discussion

A fully three-dimensional, wind-forced equatorial model is used to study the effects of the strong near-surface equatorial pycnocline on energy transmission of periodic Kelvin waves into the deep ocean. The annual equatorial Kelvin waves forced by a patch of zonal wind are isolated from the complete response, and their energy transmission into the deep ocean is

investigated as a function of forcing geometry, pycnocline strength and structure, and the amplitude of deep-ocean mixing. In order to eliminate complications due to reflected Rossby waves, solutions are found in an unbounded basin.

Solutions form well-defined beams of energy that propagate through realistic thermoclines with surprisingly little reflection. The structure and strength of the pycnocline determines the characteristics of upper-ocean reflections. Secondary beams (formed from reflected radiation) eventually ensure that all energy propagates out of the upper ocean, so that none remains trapped there. Vertical mixing damps the beams in the direction of their propagation and stretches their longitudinal extent. If mixing is sufficiently strong, the solutions lose their beamlike character and appear as surface-trapped signals. Horizontal mixing, not explicitly included in this model, is expected to affect beams in a manner similar to vertical mixing. The results of this study may help to resolve the differences between the solutions of Philander and Pacanowski (1981) and of McCreary (1984). The presence of strong frictional damping may be responsible for the apparent surface trapping in the Philander and Pacanowski study.

There are obvious limitations to this model. The model does not allow for the interaction of the waves with the strong sheared currents of the equatorial region. The background stratification varies only in the vertical, so that the model pycnocline has no zonal or meridional slope. There are no meridional
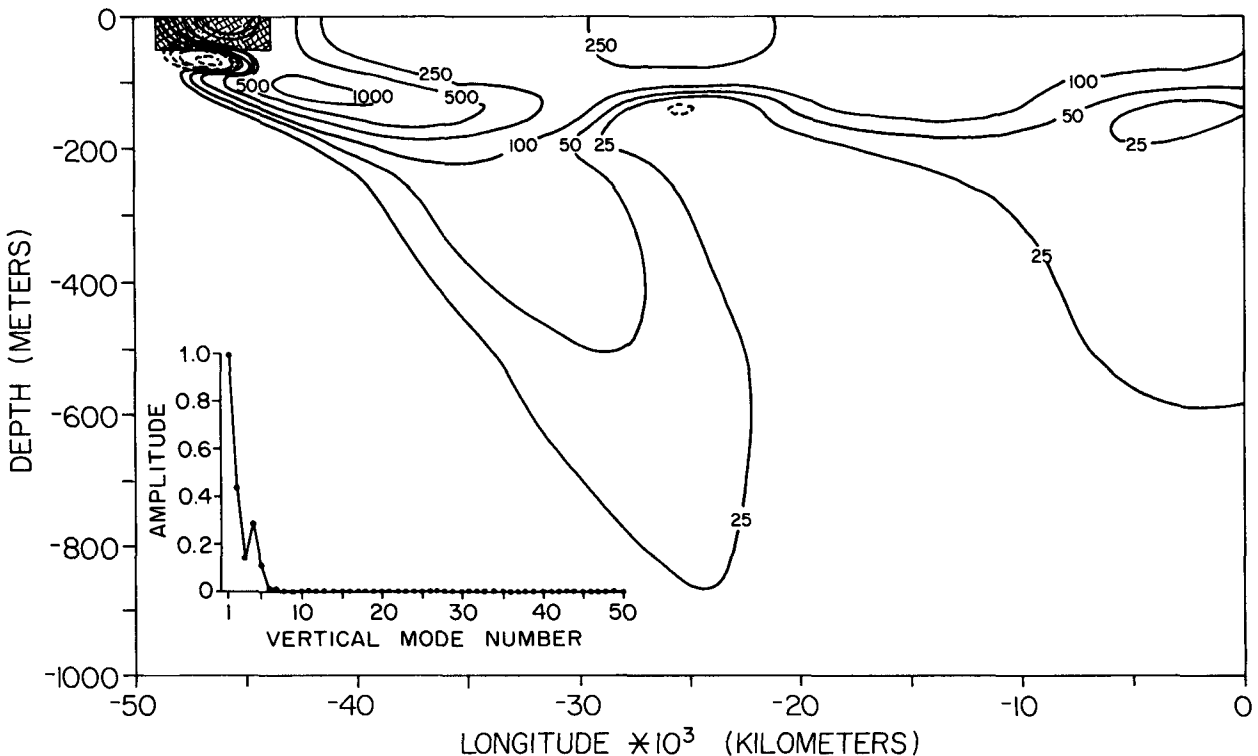

Fig. 13. As in Fig. 11, except with the mixing coefficients of Fig. 12.
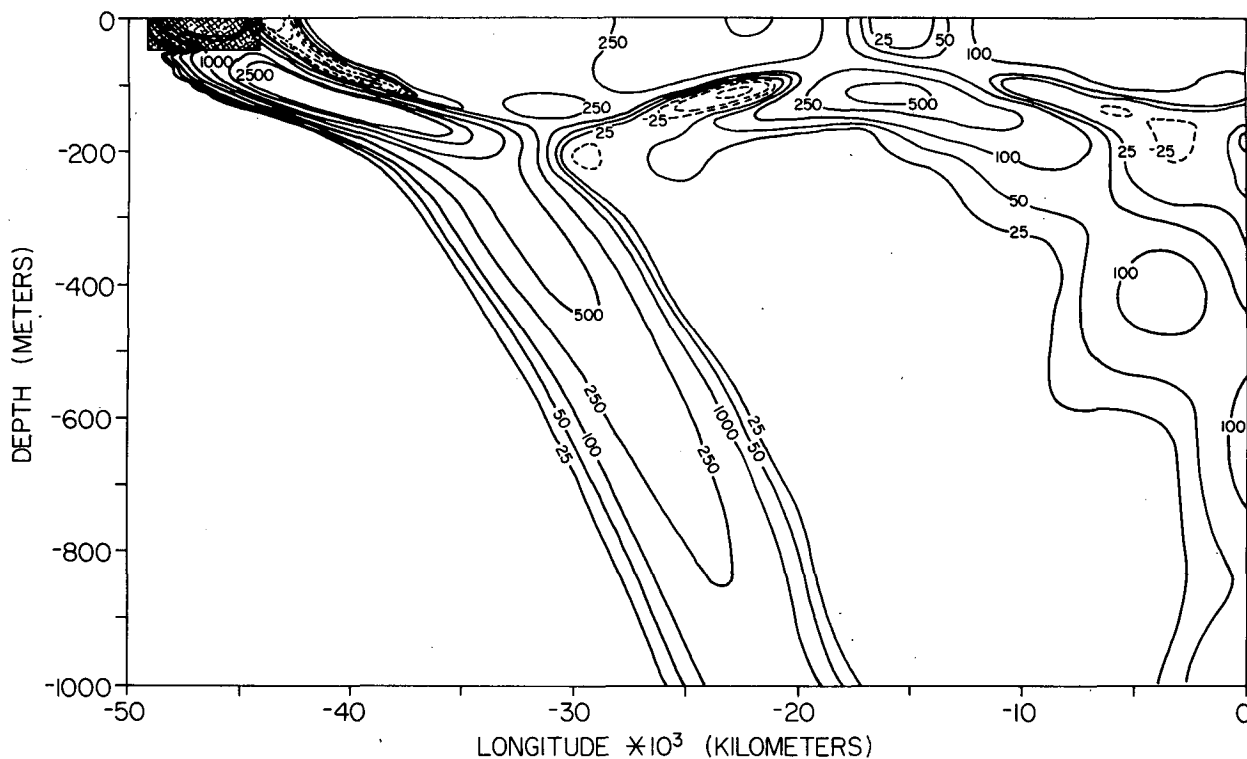
FIG. 14. As in Fig. 13, except that the mixing coefficients of Fig. 12 are reduced by an order of magnitude.

boundaries, and therefore we have eliminated the Rossby wave reflections which were the route by which the solutions of McCreary (1984) generated deep equatorial energy. Work is currently underway to overcome these limitations. In spite of these, we believe that this model does successfully isolate important dynamics involved in the propagation of energy into the deep equatorial ocean. We expect that these solutions will be useful for interpreting the response of more sophisticated equatorial models as well as an aid in understanding observations.

REFERENCES

Eriksen, C. C., 1980: Evidence for a continuous spectrum of equatorial waves in the Indian Ocean. *J. Geophys. Res.*, 85, 3285-3303.
——, 1981: Deep currents and their interpretation as equatorial waves in the western Pacific Ocean. *J. Phys. Oceanogr.*, 11, 48-70.
Hayes, S. P., 1981: Vertical finestructure observations in the eastern equatorial Pacific. *J. Geophys. Res.*, 86(C11), 10893-10999.
——, and H. B. Milburn, 1980: On the vertical structure of velocity in the eastern equatorial Pacific. *J. Phys. Oceanogr.*, 10, 633-635.
Leetmaa, A., and P. F. Spain, 1981: Results from a velocity transect along the equator from 125 to 159 W. *J. Phys. Oceanogr.*, 11, 1030-1033.
Lukas, R., and E. Firing, 1985: The annual Rossby wave in the central equatorial Pacific Ocean. *J. Phys. Oceanogr.*, 15, 55-67.
Luyten, J. R., 1982: Equatorial current measurements. I: Moored observations. *J. Mar. Res.*, 40, 19-41.
——, and J. C. Swallow, 1976: Equatorial undercurrents. *Deep-Sea Res.*, 23, 999-1001.
——, and D. H. Roemmich, 1982: Equatorial currents at semiannual period in the Indian Ocean. *J. Phys. Oceanogr.*, 12, 406-413.
McCreary, J. P., 1981: A linear stratified ocean model of the equatorial undercurrent. *Phil. Trans. Roy. Soc. London,* A298, 603-635.
——, 1984: Equatorial beams. *J. Mar. Res.,* 42, 395-430.
McPhaden, M. J., 1981: Continuously stratified models of the steady state equatorial ocean. *J. Phys. Oceanogr.*, 11, 337-354.
Philander, S. G. H., 1978: Forced oceanic waves. *Rev. Geophys. Space Phys.*, 16(1), 15-46.
——, and R. C. Pacanowski, 1980: The generation of equatorial currents. *J. Geophys. Res.*, 85, 1123-1136.
——, and ——, 1981: Response of equatorial oceans to periodic forcing. *J. Geophys. Res.*, 86(C3), 1903-1916.
Rothstein, L. M., 1984: A model of the equatorial sea surface temperature field and associated circulation dynamics. *J. Phys. Oceanogr.*, 13, 1875-1892.
Weisberg, R. H., and A. M. Horigan, 1981: Low-frequency variability in the equatorial Atlantic. *J. Phys. Oceanogr.*, 11, 913-920.
Wyrtki, K., E. Firing, D. Halpern, R. Knox, G. J. McNally, W. C. Patzert, E. D. Stroup, B. A. Taft and R. Williams, 1981: The Hawaii-to-Tahiti Shuttle Experiment. *Science,* 211, 22-28.